energies

MDPI

Article

Virtual Inertia Adaptive Control Strategy of ESU in DC Microgrid

Tao Wang [1,2], Hongshan Li [3], Taiyu Wang [3], Meng Liu [4], Tong Zhu [3] and Hongchen Liu [1,*]

[1] Department of Electrical Engineering, Harbin Institute of Technology, Harbin 150001, China
[2] State Grid Weihai Supply Company, Weihai 264200, China
[3] Department of New Energy, Harbin Institute of Technology at Weihai, Weihai 264200, China
[4] Electric Power Research Institute, State Grid Shandong Electric Power Company, Jinan 25000, China
* Correspondence: fenmiao@hit.edu.cn

Abstract: With the increasingly obvious DC characteristics at both ends of the source and load sides of the low-voltage distribution network, the application scenarios of low-voltage DC microgrid gradually appear. Compared with the AC system, the DC microgrid has the characteristics of low inertia, weak damping, and poor anti-disturbance capabilities, all of which are important for improving operational stability. A virtual inertia adaptive control approach for fast-tracking energy storage under varied disturbances is presented using energy storage as a virtual inertia unit. Firstly, a stability analysis model including constant power load is constructed for the low-voltage DC microgrid; then, the control logic of the virtual inertia of the energy storage system is designed. Finally, the corresponding model is built in MATLAB/SIMULINK and the experiment platform to verify the correctness and effectiveness of the proposed control strategy.

Keywords: energy storage system; static stability analysis; virtual inertia control; constant power load

Citation: Wang, T.; Li, H.; Wang, T.; Liu, M.; Zhu, T.; Liu, H. Virtual Inertia Adaptive Control Strategy of ESU in DC Microgrid. *Energies* **2022**, *15*, 6112. https://doi.org/10.3390/en15176112

Academic Editor: Anastasios Dounis

Received: 25 May 2022
Accepted: 18 August 2022
Published: 23 August 2022

1. Introduction

With the strategic goals of "Dual Carbon" and "New Power System", applications such as the zero-carbon and low-carbon elements represented by distributed photovoltaics, electric vehicle charging piles, and distributed energy storage will thrive in the microgrid. It will result in large-scale, disorderly, and decentralized access to the low-voltage distribution network, posing serious difficulties to its current management and control systems [1–3]. The above zero-carbon and low-carbon elements listed above all exhibit DC properties. To perform the orderly management and active control of DC-type power sources, loads, and energy storage elements, partial networking is carried out through low-voltage DC. This is an effective way to improve the coordination and interaction of low-voltage sources, power grids, loads, and energy storage, which achieves large-scale local consumption of distributed clean energy and reliable power supply for loads [4].

Although the low-voltage DC microgrid has the technical advantages of simple control objective and high conversion efficiency, it contains a constant power load (CPL) and converter with constant power control, both of which have a negative impedance characteristic, which is detrimental to the system's stable operation under disturbance [5,6]. Therefore, the research concentrates on the virtual damping or inertia control, and the low-voltage DC microgrid's stability modeling analysis. The energy storage unit (ESU) can be regarded as a first-order inertia loop, with control research focusing on how to improve the system's equivalent inertia and effectively cope with powerful impacts. Refs. [7–9] measured the power disturbance, and then decomposed the middle- and high-frequency components by the frequency domain decomposition method as the charging and discharging instructions of energy storage to stabilize the fluctuation. Ref. [10] proposed a parallel-droop control strategy based on virtual impedance to realize the distributed coordination of different ESUs. Furthermore, Refs. [11,12] distributed the transient power under disturbance based on the ratio of the nominal capacity of each ESU but ignored the impact of the state of charge

(SOC) on the transient power support. When the ESU has a low SOC but a big nominal capacity, the power distributed does not match the actual charging and discharging capacity, making it difficult to trace system disturbances, compromising system stability. In [13], an ESU charge and discharge strategy based on switching control retained its SOC within [0.3, 0.7] to realize transient power distribution. These works mentioned are generalized as being result oriented in that they study the transient control of single or multiple ESUs under disturbance. Conversely, the cause-oriented ones conduct modeling analysis and adaptive control of the virtual inertia provided by energy storage in the transient process, thus there has been no investigation into the nature of low inertia and weak damping in the system.

Setting suitable values for key parameters in the control loop is critical for achieving the optimal transient control impact. In addition, the parameter setting is usually obtained through system stability modeling and sensitivity analysis. The stability analysis of the DC microgrid system includes static stability, small disturbance stability, and large disturbance stability [14,15]. The most extensively utilized approach at the moment is small disturbance stability analysis. The impedance approach and the state-space method are also used in small disturbance stability analysis. Ref. [16,17] established an input and output impedance analysis model for a common DC bus microgrid, performed qualitative analysis on the sensitivity of important parameters such as sag using the Middlebrook impedance ratio criteria, and finally specified the parameter's tolerable value range using the Nyquist curve. However, it is unclear if various converters are separated into input or output impedance in a DC microgrid with a multi-segment bus layout, and certain converters may display distinct impedance characteristics due to different operating modes. In order to acquire the dominating poles of the system, a state-space model was built in [18,19], and then an appropriate value range was achieved by root locus analysis of important parameters. Although the state-space technique may handle the challenge of modeling a multi-bus complex system, it is more difficult to model and calculate than the impedance method.

To address the above issues, this paper firstly elaborates the system structure and configuration on which a virtual inertia control model of ESU is established to derive the virtual inertia configuration in the control process and the distribution scheme among multiple ESUs. Then the system stability analysis model is established, and the key parameters in the virtual inertia are adjusted. The correctness and effectiveness of the proposed control strategy are verified at two levels: time domain simulation and experimental platform construction, respectively.

2. System Structure and Mathematical Modeling

According to their functions or external control features, the internal units of the DC microgrid may be split into two types: (1) Balancing unit, which is the equipment that provides the DC microgrid with stable voltage support. It is usually a microgrid's grid-connected DC/AC converter or an ESU grid-connected DC/DC converter. (2) Power unit, which is the power-output unit that follows the outer loop reference. In general, it is the load grid-connected DC/DC and photovoltaic grid-connected DC/DC grid-connected converter. In some operating modes, the grid-connected DC/DC converter for energy storage can also be used as a power unit, as shown in Figure 1. The system operation mode is divided into the grid-connected operation mode and the off-grid operation mode. The control strategies and attributes of each unit under different operation modes are shown in Table 1. When the microgrid operates in grid-connected mode, the grid-connected voltage source converter (VSC) is set as the balance unit to control the constant DC voltage, and ESU acts as the power unit to eliminate the power difference in the system or suppress power fluctuations, which is a constant power control in essence. When the microgrid operates in the off-grid mode, grid-connected VSC stops operating. At this time, multiple distributed energy storage systems operate in the droop control strategy to share the power variation in the system and maintain voltage stability. Here, energy storage is used as the inertia support unit, and the super capacitor with high power density is selected as energy storage

unit, which is collectively referred to as ESU below. Compared with energy-based energy storage, it can release high energy in a short time to cope with all kinds of disturbances, and at the same time, its long cycle life can cope with frequent charging/discharging command switching when it carries out leveling fluctuations. As for the inner and outer loop control strategies of power and energy storage grid-connected DC/DC converters, there is no difference between the two basic control block diagrams.

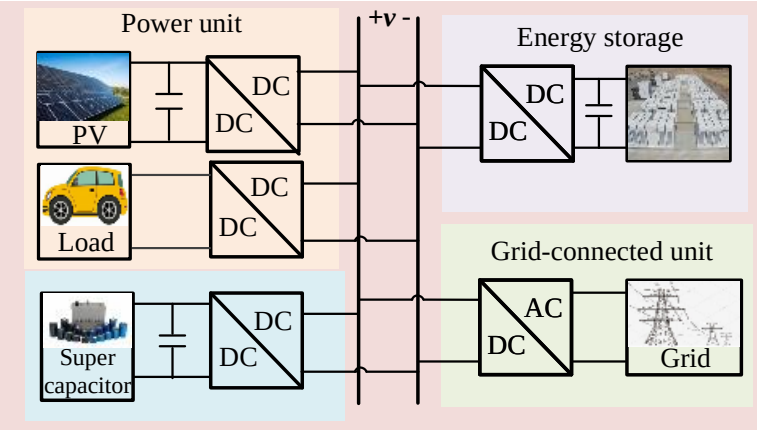

Figure 1. Topological structure of DC microgrid system.

Table 1. Operating status of each unit of DC microgird.

Operating Mode	Unit	Control Mode	Unit Attribute
Grid-connected mode	Grid-connected VSC	Droop	Balance unit
	ESU	Constant power	Power unit
	Photovoltaic	MPPT	Power unit
	Load	Constant power	Power unit
Off-grid mode	Grid-connected VSC	/	/
	ESU	Droop	Balance unit
	Photovoltaic	MPPT	Power unit
	Load	Constant power	Power unit

3. Adaptive Control Strategy of Virtual Inertia of Energy Storage Unit

3.1. Basic Control Strategy of ESU

ESU bidirectional DC-DC converters can operate in either boost or buck mode and provide bidirectional power delivery. They are usually applied as converters in energy storage systems that are linked to the power grid. The ESU operates in the constant power control mode when connected to the grid, which means that the constant low voltage or constant current control is utilized to charge and discharge according to the required power. In off-grid mode, it operates in droop control mode to regulate the high voltage; in the two extreme cases of power saturation and severe power scarcity, the ESU may also operate in idle mode. The working mode selection and control block diagram of ESU are shown in Figures 2 and 3.

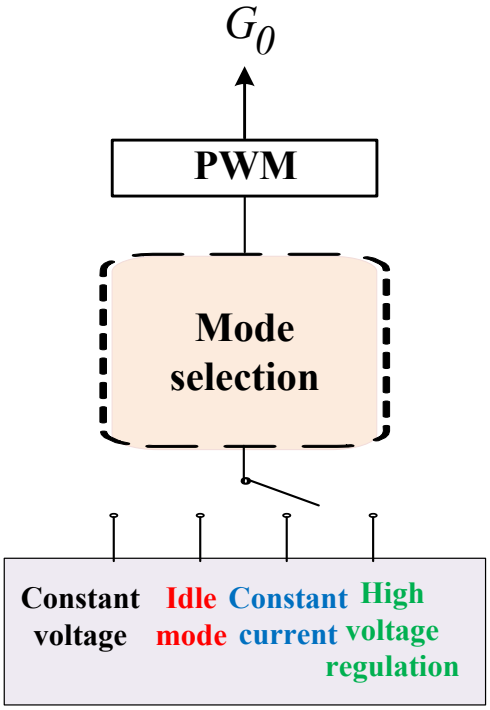

Figure 2. Different control modes of ESU.

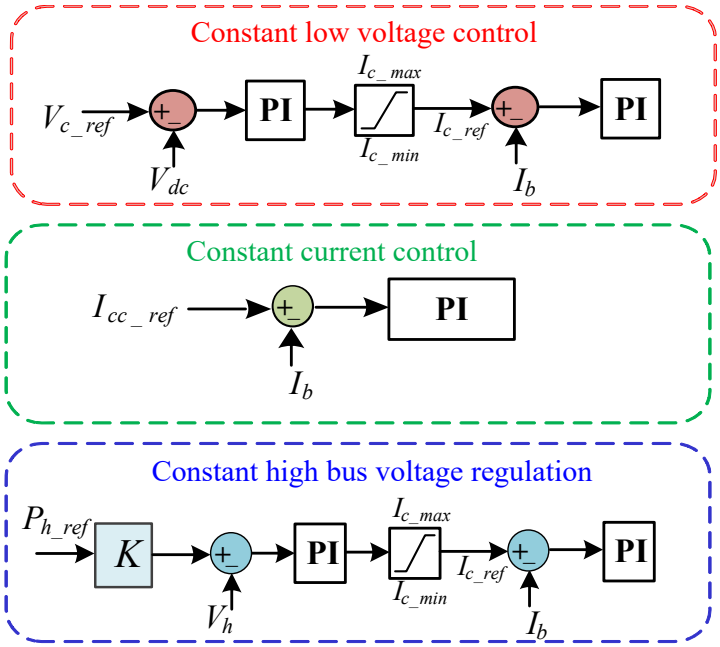

Figure 3. Control block diagram of ESU under different modes.

3.2. Virtual Inertia Control Strategy of ESU

The grid-connected VSC controls the voltage in the grid-connected mode system by drooping. Droop is simply a dampening control that cannot monitor disturbances with zero delays. To enhance this, the energy storage control approach is modified to detect the disturbance in VSC response first, releasing inertia promptly to increase system transient performance and assure stability. The continuous low voltage charge and discharge control technique is chosen as the foundation, and the design concept is as follows: the voltage per unit value of the ESU side equals the voltage per unit value of the DC bus side. This assures that ESU is 'directly' connected to the grid. The improved control strategy is shown in Figure 4.

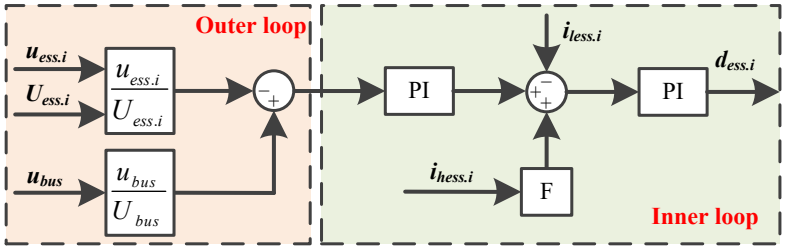

Figure 4. Improved control block diagram.

In Figure 4, $u_{c.i}$ and $U_{c.i}$ are the low-voltage side voltage and the reference voltage of ith ESU; u_{bus} and U_{bus} represent the bus voltage and bus reference voltage; $i_{lc.i}$ and $i_{hc.i}$ are the current and the bus side current of ith ESU; and $d_{c.i}$ represents the duty cycle, respectively. Feedforward control is used in inner loop control to increase the voltage dynamic consistency between the energy storage side and the bus side, where F is the feedforward coefficient. The energy storage voltage per unit value is almost equivalent to the bus voltage per unit value:

$$u_{c.i} \approx U_{c.i} \cdot u_{bus.p.u.} \tag{1}$$

where $u_{bus.p.u.}$ is bus voltage per-unit value. Equation (1) shows that $U_{c.i}$ can reflect the ESU operating level and is also proportional to the amount of released inertia in the transient state. When there is a power disturbance $\Delta P_{L.p.u.}$, the DC bus voltage fluctuates as illustrated in Equation (2).

$$2\frac{C_{bus}U_{bus}^2}{2P_G}\frac{d\Delta u_{bus.p.u.}}{dt} = \Delta P_{L.p.u.} \tag{2}$$

where C_{bus} is the bus-to-ground capacitor, P_G is the reference value of $\Delta P_{L.p.u.}$ and LOM1-1, LOM3-1 begin$\frac{C_{bus}U_{bus}^2}{2P_G}$ is the inertia stored by the system. Define $H_{mg} = \frac{C_{bus}U_{bus}^2}{2P_G}$. This value is directly related to the inherent equivalent capacitance value C_{bus} at the busbar. The power per-unit value change of ESU is further derived as shown in Equation (3):

$$\begin{cases} \Delta P_{ci.pu} = -\dfrac{U_{ci}^2 C_{ci}}{P_G}\dfrac{d\Delta u_{ci}}{dt}, & \Delta u_{ci} = U_{ci}\Delta u_{bus.pu} \\ \Delta P_{ci.pu} = -2H_{ci}\dfrac{d\Delta u_{bus.pu}}{dt}, & H_{ci} = \dfrac{U_{ci}^2 C_{ci}}{2P_G} \end{cases} \tag{3}$$

where $\Delta u_{ci} = U_{ci}\Delta u_{bus.pu}$ can be considered the relationship between $\Delta P_{ci.pu}$ and $\Delta u_{bus.pu}$. H_{ci} characterizes the virtual inertia injected into the DC bus by the ith ESU during transient operation. During the transient operation of the system and when more than one energy storage unit is involved, there are two problems: (1) how much inertia in total needs to be allocated to ESU and according to what principle; (2) according to what principle these inertias are distributed among multiple energy storage. First of all, in addition to the inertia response of the system itself in Equation (2), the power dynamic balance of the system in the transient process also involves ESUs, the grid-connected VSC and the load changes. The PV unit in Figure 1 is considered to have constant output power in the transient state, so it does not participate in the dynamic balance of the system power. The power dynamic balance of the system in the transient state is shown in Equation (4).

$$2H_{mg}\frac{d\Delta u_{bus.pu}}{d\Delta t} + 2sH_c \cdot \Delta u_{bus.pu} + G_{vsc} \cdot \Delta u_{bus.pu} + \Delta P_{L.pu} = 0 \tag{4}$$

where G_{vsc} is the closed-loop control transfer function of the grid-connected converter, ignoring current inner-loop dynamic effect, $G_{vsc} = k_p + \frac{k_i}{s}$. H_c is the configuration of the total virtual inertia of the ESU, which is the superposition of each subterm H_{ci}. The ex-

pression for the DC bus voltage variation is obtained by equivalently varying Equation (5) as follows:

$$\Delta u_{bus.pu} = -\frac{1}{2 \cdot H_{mg}} \cdot \frac{s}{s^2 + k_p \cdot s/2H_c + (2H_{mg} + k_i)/2H_c} \cdot \Delta P_{L.pu} \tag{5}$$

Make

$$\begin{cases} \xi = \dfrac{k_p}{2H_c} \cdot \dfrac{\sqrt{2H_c}}{2\sqrt{k_i + 2H_{mg}}} \\ \omega_n = \sqrt{\dfrac{k_i + 2H_{mg}}{2H_c}} \end{cases} \tag{6}$$

Therefore, Equation (5) can be written as

$$\Delta u_{bus.pu} = -\frac{1}{2 \cdot H_{mg}} \cdot \frac{s}{s^2 + 2\xi \cdot \omega_n \cdot s + \omega_n^2} \cdot \Delta P_{L.pu} \tag{7}$$

Equation (7) is a typical form of the second-order system, where ξ is the damping ratio, ω_n is the oscillation frequency. These two parameters determine the characteristics of the system, such as overshoot, regulation time and damping state. Taking the regulation time T_s as the inertia support time under the transient state of ESU, and then as the configuration principle of H_c, ignoring the influence of the sinusoidal function. It is considered that when the exponential function decays to the steady-state error $\Delta = 0.02$, the transient process ends, and the formula of the adjustment time T_s can be expressed as Equation (8):

$$T_s(2\%) = \frac{1}{\xi \cdot \omega_n}[4 - \frac{1}{2} \cdot \ln 1 - \xi^2] \approx \frac{4}{\xi \cdot \omega_n} \tag{8}$$

From Equations (6) and (8), the following equation can be obtained:

$$T_s = \frac{4}{\xi \cdot \omega_n} = \frac{16H_c}{k_p} \tag{9}$$

Given T_s and control parameter k_p, the total virtual inertia H_c can be obtained, which means ESU needs to generate inertia H_c under the matching system regulation time T_s. After determining the total inertia H_c, it is also necessary to specify how to allocate it among multiple ESUs. The principle of distribution is similar to the method of power allocation among multiple converters based on their respective capacities under parallel peer-to-peer control, which can be based on the ratio of the maximum inertia H_{cmax} of each ESU, as shown in Equation (10).

$$H_c = \frac{C_c U_c^2}{2P_G} = \frac{C_{c1} U_{c1}^2}{2P_G} + \cdots + \frac{C_{ci} U_{ci}^2}{2P_G} \tag{10}$$

The transient output power between ESUs is allocated according to the inertia ratio. The above inertia output time is matched according to the system regulation time $T_s(2\%)$, which completes the inertia and output power distribution among multiple ESUs.

3.3. Stability Calculation and Parameter Design

The maximum inertia configuration of ESU and the selection of the equivalent capacitance parameters of the DC bus will affect the stability of the system. The configuration of the maximum inertia H_{cmax} of ESU can be designed by giving the maximum step load level ΔP_{Lmax} in Equation (5). ΔP_{Lmax} needs to be calculated from the stability. The calculation of maximum load step power level belongs to the category of large disturbance stability, and the mixed potential function and stability criterion is established to set it. First, the system is equivalent to a steady state model as shown in Figure 5.

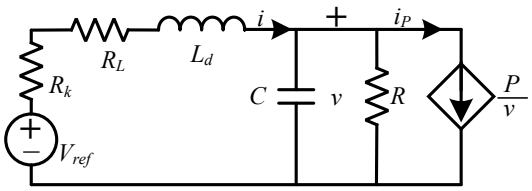

Figure 5. Equivalent circuit model of DC microgrid system.

Based on the above analysis, ignoring all converters voltage and current dynamic control, the system can be equivalent to an ideal voltage source with series resistance. The right side can be equivalent to a CPL. P is the sum of the power of power units, U_{ref} is the reference voltage of balanced unit. Based on Figure 5, the following equation can be obtained:

$$\begin{aligned} \frac{di}{dt} &= \frac{1}{L_d}\left(U_{ref} - U_{bus} - R_L i\right) \\ \frac{dU_{bus}}{dt} &= \frac{1}{C_{bus}}\left(i - \frac{U_{bus}}{R} - \frac{P}{U_{bus}}\right) \end{aligned} \tag{11}$$

where U_{bus} and i are state variables. Based on Ref. [20] for the modeling method and criterion of MPF, the MPF equations of the DC microgrid are listed as follows:

$$\begin{aligned} P(i, U_{bus}) = \int_{i_{sb}}^{i} -R_L i di + \int_{\frac{U_{sb}}{R}}^{\frac{U}{R}} -U_{bus} d\frac{U_{bus}}{R} + \int_{i_{psb}}^{i_p} -U_{bus} d\frac{P}{U_{bus}} + \int_{i_{sb}}^{i} U_{ref} di \\ + (-U_{bus})(i - \frac{P}{U_{bus}} - \frac{U_{bus}}{R}) \end{aligned} \tag{12}$$

The right side of the equation shows the current potential function of each subterm in Figure 4, and they further build LEF as shown in Equation (13).

$$F(i, U_{bus}) = (\tfrac{\lambda_1 - \lambda_2}{2}) P(i, U_{bus}) + \tfrac{1}{2L_d}(U_{ref} - U_{bus} - R_L i)^2 + \tfrac{1}{2C_{bus}}(\tfrac{U_{bus}}{R} + \tfrac{P}{U_{bus} - i})^2 \tag{13}$$

where λ_1 and λ_2 are two eigenvalues respectively, as shown in Equation (14).

$$\begin{cases} \lambda_1 = -\frac{R_L}{L_d} \\ \lambda_2 = \frac{(1/R - P/U_{bus}^2}{C_{bus}} \end{cases} \tag{14}$$

The MPF stability theorem states that when the bus voltage U_{bus} is greater than a certain minimum value $U_{bus-min}$, the partial derivative of $F(i, U_{bus})$ with respect to time will be less than zero and the system is stable. The LaSalle invariant set [21] is further introduced to portray EDA [22] of the system as shown in equation Equation (15).

$$EDA = \{(i, U_{bus}) | F(i, U_{bus}) \leq min(F_{max1}, F_{max2})\} \tag{15}$$

where F_{max1} is the value corresponding to the maximum tight set of LEF and $F_{max2} = minF(i, U_{bus-min})$. This theorem overcomes the difficulty of judging whether the LEF is positive definite. Whether the initial operating point is within the post-step operating point EDA determines the stability. The specific criteria are described as follows: operating point $x_{s1}(i_1, U_{bus1})$ estimates the region within EDA, the partial derivative of $F_(i, U_{bus})$ with respect to time is always less than zero, and the system is stable. Therefore, when the system steps from $x_{s0}(i_0, U_{bus0})$ to $x_{s1}(i_1, U_{bus1})$, the system will eventually converge to the point x_{s1} if the starting point $x_{s0}(i_0, U_{bus0})$ is within the EDA of $x_{s1}(i_1, U_{bus1})$; otherwise, the system will be unstable. This process determines $\Delta P_{Lmax.pu}$ in Equation (5). After setting the critical stability step value $\Delta P_{Lmax.pu}$, H_{cmax} is rectified by parameter sensitivity analysis.

4. Simulation Results

4.1. Comparison of Time-Domain Simulations of Reduced-Order Models

According to the parameter configuration in Table 2, the reduced-order model in Figure 5 is compared with the full-order model (switch model) in the time-domain simulation, and the results are shown Figure 6.

Table 2. Parameters of DC microgrid system.

Name	Value
Power level of balanced unit and power unit	150 kW
$C_{bus}/C_{c1}/C_{c2}$	0.1 F/8 F/8 F
Output voltage U_{ref}	400 V
Resistance R_L/Reactance L_d	0.8 Ω/36.5 mH
Parallel resistance R	90 Ω
SC reference voltage V_{ref1}	210 V
SC inductance L_1/capacitance C_1/Resistance R_1	0.7 mH/0.9 mF/22 mΩ
SC voltage loop proportional/integral coefficient	1/10
SC current loop proportional/integral coefficient	1/10
LC reference voltage V_{ref2}	40 V
LC inductance L_2/capacitance C_2/Resistance R_2	0.7 mH/0.5 mF/15 mΩ
LC voltage loop proportional/integral coefficient	1/1
LC current loop proportional/integral coefficient	1/100

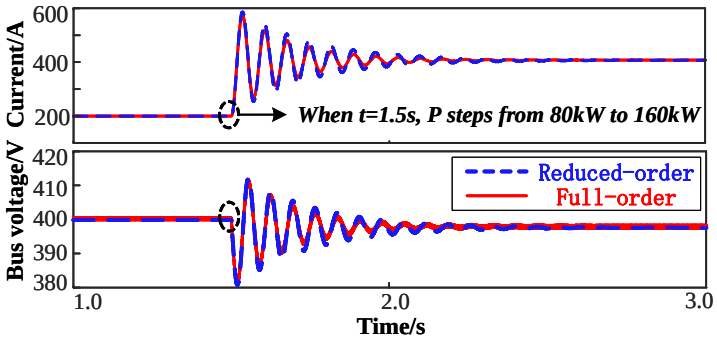

Figure 6. Time-domain simulationcomparison between reduced-order model and full-order mode.

In Figure 6, the constant load power is stepped from 80 kW to 160 kW at $t = 1.5$ s. During the transient process, the reduced-order model has almost the same dynamic characteristics as the full-order model, which proves the validity of the established reduced-order model.

4.2. Stability and Inertia Sensitivity Analysis

Given $C_{bus} = 0.1$ F, EDA and convergence under different power steps are shown in Figure 7.

In Figure 7, when the system first steps from $x_{s0} = 0$ to $x_{s1} = 100$ kW and then steps to $x_{s2} = 150$ kW, the initial point of each step is within the EDA of the end point of the step, and it is known from the previous stability criterion that the step is stable and will eventually converge to the point to be stepped (black path). If the step from $x_{s0} = 0$ to $x_{s2} = 150$ kW, initial point is not in EDA of the point to be stepped, and the stability criterion shows that x_{s0} will not converge to x_{s2} (red path) and the system will be unstable. The above analysis determines the maximum step load of the system $\Delta P_{Lmax} = 100$ kW, and the maximum configuration inertia H_{cmax} of ESU is further clarified by substituting $\Delta P_{Lmax.pu} = 0.7$ into Equation (5). The trajectory of the two characteristic roots during the change of the total output inertia H_{cmax} of ESU from 1.4 to 0.2, that is, U_c from 320 V to 560 V, is shown in Figure 8. From the results of the parameter sensitivity analysis, it can be seen that when ESU outputs inertia H_c changes from 1.4 to 0.2 ($U_{c.pu}$ from 0.8 to 1.4), the system

pole gradually approaches the imaginary axis, and when $H_{cmax} = 0.4$ ($U_{c.pu} = 1.3$), the pole is located in the imaginary axis and the system is critically stable. When the parameters change further, the pole will be located in the right half-plane and the system is destabilized. Selecting three groups of parameters $H_{cmax} = 0.4, 0.6, 0.9$, the corresponding time-domain simulation is shown in Figure 9, and the Bode plot is shown in Figure 10.

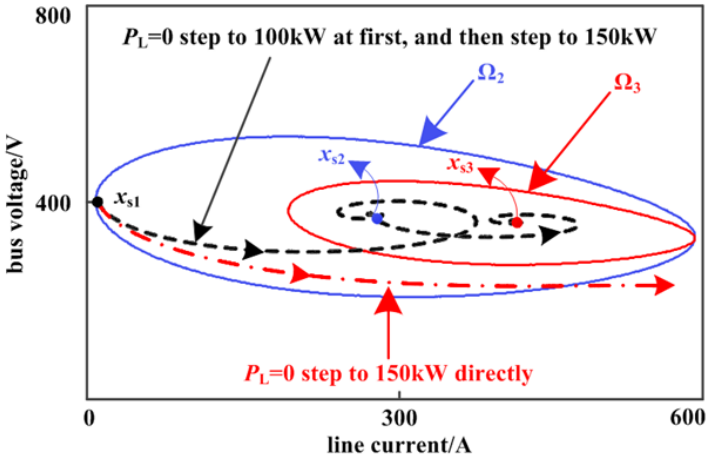

Figure 7. Time domain simulation comparison between reduced-order model and full-order mode.

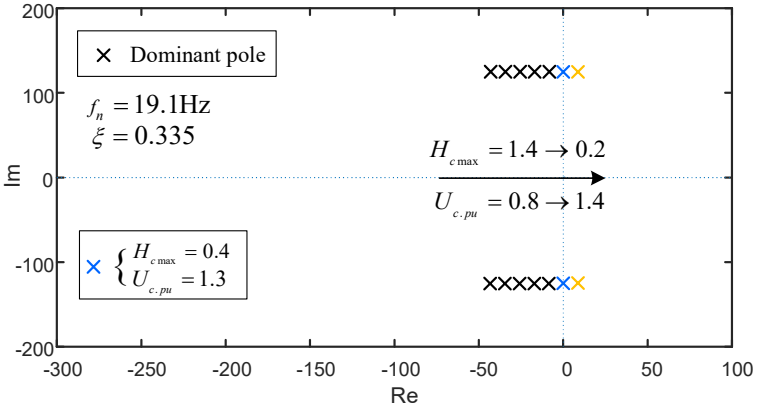

Figure 8. Parameter sensitivity analysis.

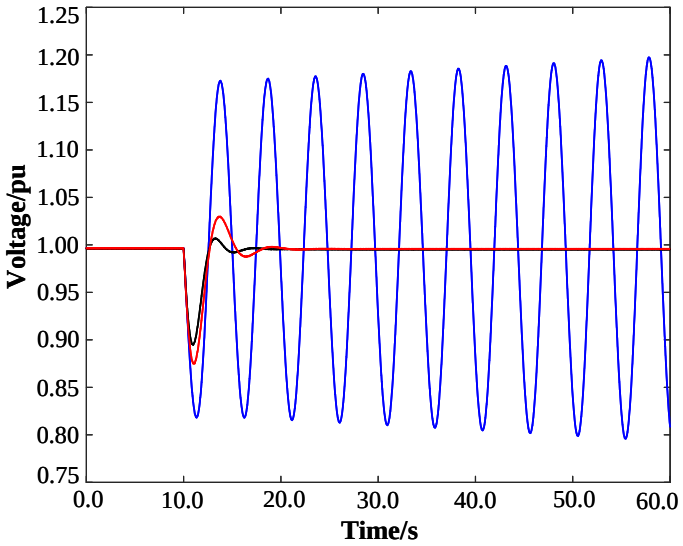

Figure 9. Time domain simulation result. Blue, red and black curves represent $H_{cmax} = 0.4$, $H_{cmax} = 0.6$ and $H_{cmax} = 0.9$ respectively.

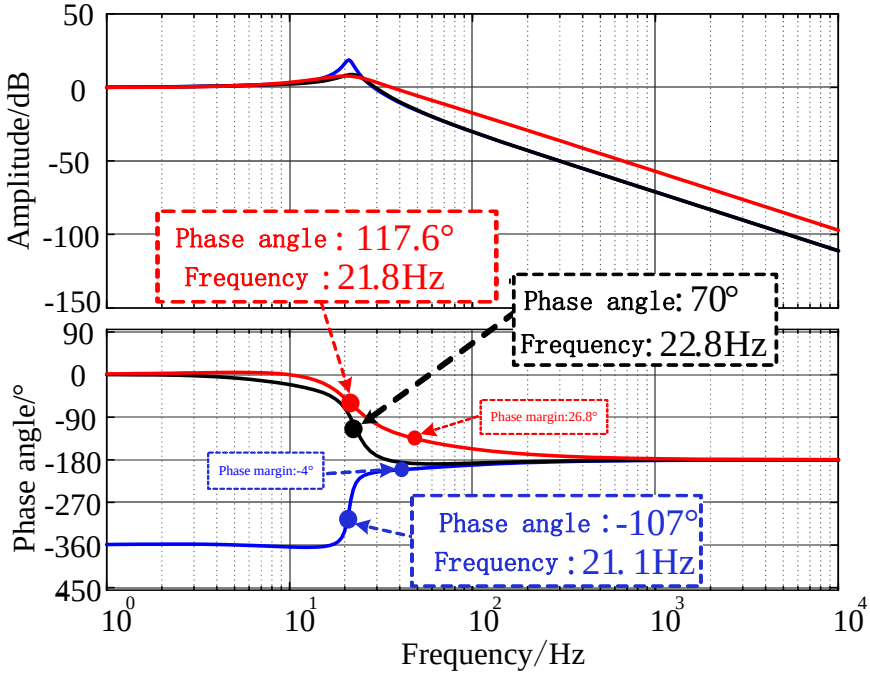

Figure 10. Bode plot. Blue, red and black curves represent $H_{cmax} = 0.4$, $H_{cmax} = 0.6$ and $H_{cmax} = 0.9$ respectively.

$H_{cmax} = 0.4, 0.6, 0.9$ correspond to the blue, red, and black curves, respectively. It can be seen that when $H_{cmax} = 0.4$, the system is in critical stability and close to constant amplitude oscillation, which is consistent with the stability analysis results. And with the continuous increase of inertia, the transient response time of the system is shorter, and it can enter a stable state faster (comparison of red and black curves). From Figure 10, with the increase of inertia, the phase angle margin increases from $-4°$ to 26.8° (damping is positive), and the system oscillation disappears. Although larger inertia leads to faster response, it may cause system to have no overshoot, acting as over-damping. Therefore, it is not that the larger inertia, the better, but need to achieve a moderate matching of inertia. Under the above-mentioned disturbance conditions, the matching inertia is selected as $H_{cmax} = 0.9$. In this paper, the two ESUs configuration scheme is used, and the maximum inertia ratio of the two is 2:1.

4.3. Time-Domain Simulation Analysis of ESU Inertia Output Distribution

Given $T_s = 10$ s, the required $H_c = 0.6$ at this T_s is calculated by Equation (9). The two ESUs are distributed according to the maximum inertia ratio $H_{c1} = 0.4$ and $H_{c2} = 0.2$. Here, T_s can be calculated under actual oscillation according to the waveform playback, analytical method or fast Fourier analysis, which is not repeated in this paper. Further, according to Equation (10), $U_{c1} = 122.5$ V and $U_{c2} = 86.6$ V, the transient power distribution is $\Delta P_{esspu.1}$:$\Delta P_{esspu.2}$ = 2:1, the simulation results are shown in Figures 11–13. When $t = SI10$ s and $t = 30$ s, the load is suddenly increased by 0.6 p.u. and decreased by 0.6 p.u. respectively. During the transient process of the system, the two ESUs output inertia according to the inertia distribution ratio, which cooperates with the VSC in response time. The voltage is controlled within a reasonable range, and the actual process is consistent with the theoretical analysis.

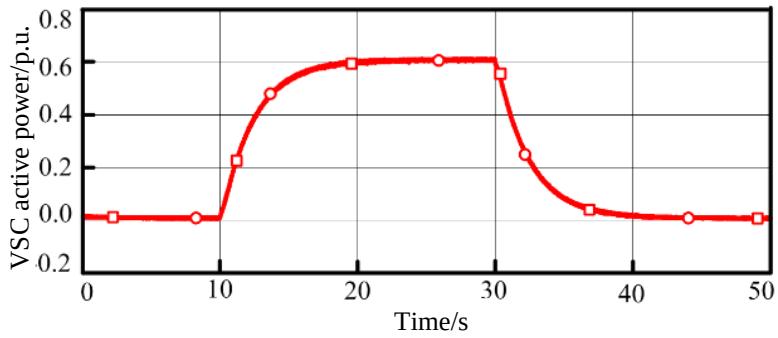

Figure 11. VSC active power curve.

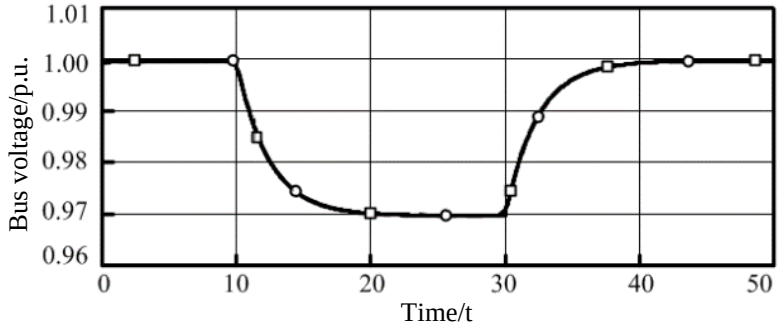

Figure 12. Bus voltage curve.

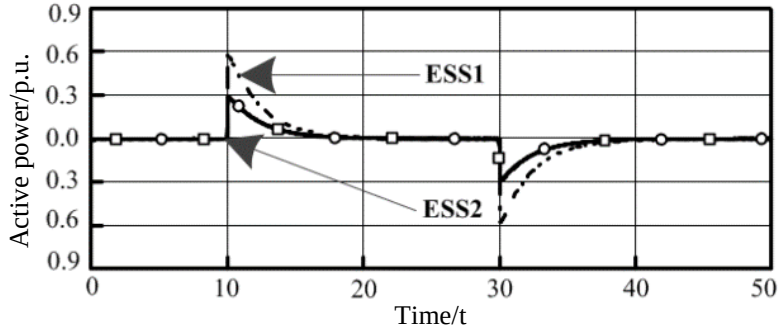

Figure 13. ESU output curve.

4.4. Experimental Verification

Based on the above time-domain simulation verification, the DC microgrid experimental platform is further built, as shown in Figure 14. Module S is a TopCon series bidirectional DC source module, 32 kW × 8500 V. It can be used as PV, ESU and DC load. Module B is the system 400 V, single-pole DC bus. Module C is the configuration control management system, which realizes the function of communication manager while effectively controlling the microgrid from millisecond level to hourly level. Module vsc is the DC microgrid grid-connected bidirectional converter. Module pv is the PV grid-connected converter. Modules sc1 and sc2 simulate the grid-connected bidirectional converter of energy storage units 1 and 2 respectively. Module L is the CPL grid-connected converter. In the experiment, the simulation is carried out according to the working conditions in the time-domain simulation. The response of ESU and the power curve of each module are shown in Figure 15.

In Figure 15, the experimental system simulates the sudden increase and decrease in the 90 kW DC load at $t = 5$ s and $t = 15$ s, respectively. ESU and the grid-connected VSC perform time sequence coordination when the load is disturbed, and ESU takes the lead in responding to provide inertia support according to the proportion. ESU 1 and ESU 2

respectively support a maximum power of 60 kW and 30 kW. The proposed strategy is verified to be correct and effective.

Figure 14. DC microgrid experimental platform.

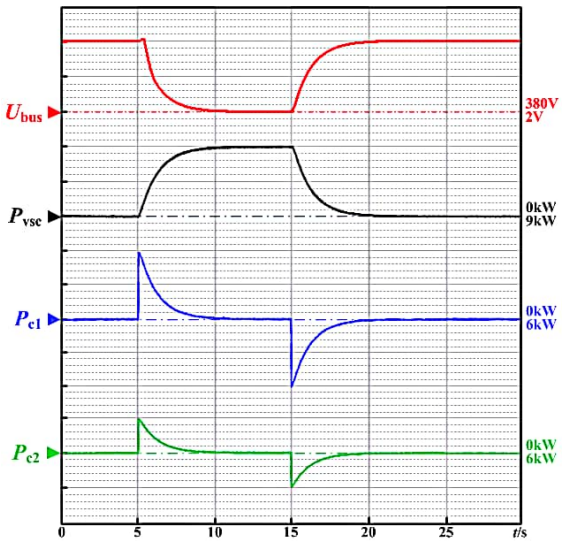

Figure 15. Experimental results.

5. Conclusions

In this paper, an inertia adaptive control method under decentralized configuration is proposed for ESU in DC microgrid. This method takes advantage of the fast response characteristics of the energy storage inertia unit and quickly matches the inertia when the system is disturbed so as to improve the system performance in transient state. Meanwhile, a reduced-order equivalent model of the system is constructed, and the key parameters in inertia control of ESU are set through stability analysis. Finally, the correctness and effectiveness of the proposed strategy are verified by time-domain simulation and experiments. The set of ESU inertia control methods designed in this paper can be extended to ESU cluster systems, providing a practical solution for stable control of DC microgrids and distributed ESU cluster systems.

Author Contributions: Conceptualization, T.W. (Tao Wang); Investigation, T.Z.; Resources, M.L.; Visualization, H.L. (Hongchen Liu); Writing—original draft, T.W. (Taiyu Wang); Writing—review & editing, H.L. (Hongshan Li). All authors have read and agreed to the published version of the manuscript.

Funding: This work is supported by the National Natural Science Foundation of China (No. 61773137), the Natural Science Foundation of Shandong Province (No. ZR2019MF030).

Institutional Review Board Statement: Not applicable.

Informed Consent Statement: Not applicable.

Data Availability Statement: Not applicable.

Conflicts of Interest: The authors declare no conflict of interest.

Abbreviations

The following abbreviations are used in this manuscript:

ESU	Energy storage unit
DC	Direct current
SOC	State of charge
VSC	Voltage source converter
MPPT	Maximum power point tracking
DG	Distributed generator
PV	Photovoltaic
SC	Source converter
LC	Load converter
CPL	Constant power load
VCC	Voltage and current closed-loop control
MPF	Mixed potential function
LEF	Lyapunov-type energy function
EDA	Estimated domain of attraction

References

1. Li, Q.; Zhang, J. Solutions of voltage beyond limits in distribution network with distributed photovoltaic generators. *Autom. Electr. Power Syst.* **2015**, *39*, 117–123.
2. Walling, R.; Saint, R.; Dugan, R.C.; Burke, J.; Kojovic, L.A. Summary of distributed resources impact on power delivery systems. *IEEE Trans. Power Deliv.* **2008**, *23*, 1636–1644. [CrossRef]
3. Yuan, K.; Song, Y.; Li, J.; Sun, C.; Wu, Z.; Yuan, B.; Xue, Z.; Jin, X. Harmonic Characteristics of Distributed Generation and Electric Vehicle Supplying Access to the Grid. *Proc. CSEE* **2018**, *38*, 54.
4. Liu, H.; Xiong, X.; Ji, Y.; Wu, M.; rui Li.; Sun, L. Cluster Control Research of DC-type Distributed Generators Based on Multi-microgrids Technology under DC Distribution System. *Proc. CSEE* **2019**, *39*, 9.
5. Li, X.; Guo, L.; Wang, C.; Li, Y. Key technologies of DC microgrids: An overview. *Proc. CSEE* **2016**, *36*, 2–17.
6. Li, Z.; Kong, L.; Pei, W. Analyses of Stability Criterion and Key Factors of DC Microgrid Under Large Disturbance. *High Volt. Eng.* **2019**, *45*, 3993–4002.
7. Bellache, K.; Camara, M.B.; Dakyo, B. Transient power control for diesel-generator assistance in electric boat applications using supercapacitors and batteries. *IEEE J. Emerg. Sel. Top. Power Electron.* **2017**, *6*, 416–428. [CrossRef]
8. Jin, Z.; Meng, L.; Guerrero, J.M.; Han, R. Hierarchical control design for a shipboard power system with DC distribution and energy storage aboard future more-electric ships. *IEEE Trans. Ind. Inform.* **2017**, *14*, 703–714. [CrossRef]
9. Chen, X.; Zhou, J.; Shi, M.; Yan, L.; Zuo, W.; Wen, J. A novel virtual resistor and capacitor droop control for HESS in medium-voltage DC system. *IEEE Trans. Power Syst.* **2019**, *34*, 2518–2527. [CrossRef]
10. He, L.; Li, Y.; Guerrero, J.M.; Cao, Y. A comprehensive inertial control strategy for hybrid AC/DC microgrid with distributed generations. *IEEE Trans. Smart Grid* **2019**, *11*, 1737–1747. [CrossRef]
11. Xu, Q.; Hu, X.; Wang, P.; Xiao, J.; Tu, P.; Wen, C.; Lee, M.Y. A decentralized dynamic power sharing strategy for hybrid energy storage system in autonomous DC microgrid. *IEEE Trans. Ind. Electron.* **2016**, *64*, 5930–5941. [CrossRef]
12. Lin, P.; Wang, P.; Xiao, J.; Wang, J.; Jin, C.; Tang, Y. An integral droop for transient power allocation and output impedance shaping of hybrid energy storage system in DC microgrid. *IEEE Trans. Power Electron.* **2017**, *33*, 6262–6277. [CrossRef]
13. Chen, J.; Song, Q. A decentralized dynamic load power allocation strategy for fuel cell/supercapacitor-based APU of large more electric vehicles. *IEEE Trans. Ind. Electron.* **2018**, *66*, 865–875. [CrossRef]

14. Wang, X.; Li, X. Small-signal stability analysis of islanded DC microgrid with wind power. *Electr. Power Autom. Equip.* **2017**, *37*, 92–99.
15. Li, P.; Li, X.; Wang, C.; Guo, L.; Peng, K.; Zhang, Y.; Wang, Z. Review of stability analysis model and mechanism research of medium- and low-voltage flexible DC distribution system. *Electr. Power Autom. Equip.* **2021**, *41*, 3–21.
16. Vasquez, J.C.; Guerrero, J.M.; Miret, J.; Castilla, M.; De Vicuna, L.G. Hierarchical control of intelligent microgrids. *IEEE Ind. Electron. Mag.* **2010**, *4*, 23–29. [CrossRef]
17. Zhi, N.; Zhang, H.; Xiao, X.; Yang, J. System-level stability analysis of DC microgrid with distributed control strategy. *Proc. CSEE* **2016**, *36*, 368–378.
18. Herrera, L.; Yao, X. Computation of stability metrics in DC power systems using sum of squares programming. In Proceedings of the 2017 IEEE 18th Workshop on Control and Modeling for Power Electronics (COMPEL), Stanford, CA, USA, 9–12 July 2017; pp. 1–5.
19. Loop, B.P.; Sudhoff, S.D.; Żak, S.H.; Zivi, E.L. Estimating regions of asymptotic stability of power electronics systems using genetic algorithms. *IEEE Trans. Control Syst. Technol.* **2009**, *18*, 1011–1022. [CrossRef]
20. Li, X.; Liu, N.; Song, X. Large-signal stability criteria of AC/DC hybrid microgrid based on AC constant power loads. *High Volt. Eng.* **2021**, *47*, 11.
21. Zhang, Y.; Wang, C.; Zhang, H. Chaos control of parameter magnet synchronous motor based on finite time LaSalle invariant set. *J. Syst. Simul.* **2020**, *32*, 8.
22. Li, X.; Wang, Z.; Guo, L. Transient stability analysis of PLL synchronization in Weak-Grid-Connected VSCs based on the largest estimated domain of attraction. *Proc. CSEE* **2022**, *42*, 29–38. [CrossRef]